Collision of continental corner from 3-D numerical modeling

Zhong-Hai Li [a,*], Zhiqin Xu [a], Taras Gerya [b,c], Jean-Pierre Burg [d]

[a] *State Key Lab of Continental Tectonics and Dynamics, Institute of Geology, Chinese Academy of Geological Sciences, Beijing, China*
[b] *Institute of Geophysics, Department of Earth Sciences, ETH-Zurich, Switzerland*
[c] *Geology Department, Moscow State University, Moscow, Russia*
[d] *Geological Institute, Department of Earth Sciences, ETH and University Zurich, Switzerland*

A B S T R A C T

Continental collision has been extensively investigated with 2-D numerical models assuming infinitely wide plates or insignificant along-strike deformation in the third dimension. However, the corners of natural collision zones normally have structural characteristics that differ from linear parts of mountain belt. We conducted 3-D high-resolution numerical simulations to study the dynamics of a continental corner (lateral continental/oceanic transition zone) during subduction/collision. The results demonstrate different modes between the oceanic subduction side (continuous subduction and retreating trench) and the continental collision side (slab break-off and topography uplift). Slab break-off occurs at a depth (⩽100 km to ∼300 km) that depends on the convergence velocity. The numerical models produce lateral extrusion of the overriding crust from the collisional side to the subduction side, which is also a phenomenon recognized around natural collision of continental corners, for instance around the western corner of the Arabia–Asia collision zone and around the eastern corner of the India–Asia collision zone. Modeling results also indicate that extrusion tectonics may be driven both from above by the topography and gravitational potentials and from below by the trench retreat and asthenospheric mantle return flow, which supports the link between deep mantle dynamics and shallower crustal deformation.

© 2013 Elsevier B.V. All rights reserved.

1. Introduction

Continental subduction and collision normally follows oceanic subduction under the combined convergent forces of 'ridge push' and/or oceanic 'slab pull' (e.g., Turcotte and Schubert, 2002). Besides the systematic geological/petrological studies of recent continental collision zones (e.g., Alpine–Zagros–Himalayan belt), analogue (e.g., Chemenda et al., 1995, 1996, 2000; Boutelier et al., 2004) and numerical models (e.g., Beaumont et al., 2001, 2009; Burov et al., 2001; Liu et al., 2004; Toussaint et al., 2004; Burg and Gerya, 2005; Sobolev and Babeyko, 2005; Gerya et al., 2008a; Yamato et al., 2007, 2008; Warren et al., 2008; Li and Gerya, 2009; Li et al., 2010, 2011; Chen et al., 2013) are also widely used and become more and more substantial to investigate continental subduction/collision processes. The numerical tectonic styles of continental subduction/collision can be either "one-sided" (overriding plate does not subduct) or "two-sided" (both plates subduct together) (Tao and O'Connell, 1992; Pope and Willett, 1998; Faccenda et al., 2008; Warren et al., 2008; Li et al., 2011). Several other possibilities such as thickening, slab drips (e.g., Toussaint et al., 2004) and slab break-off (e.g., Duretz et al., 2011, 2012; Van Hunen and Allen, 2011) have been put forward. The one-sided style can be

further divided into steep (high angle) and flat (low angle) subduction/collision zones, resulting in different structures, stress states and deformation styles in the converging plates as well as different metamorphic pressure conditions of the exhumed wedge rocks (e.g., Li et al., 2011).

However, most of the models mentioned in the previous section are based on the 2-D regime, assuming that the plate is infinitely wide or that along-strike deformation in the third dimension can be neglected. 2-D models are indeed relevant to study the general processes and dynamics in the continental subduction channels and/or the interior of the continental collision zones, but far from curvilinear areas such as the continental corners. Recent 3-D numerical models of oceanic subduction, without continental collision, revealed different characteristics and scaling laws between the lateral edges and the interior of subducting slabs (e.g., Schellart et al., 2011; Li and Ribe, 2012). In nature, convergent continents have borders with transition to oceanic plates or to other continents. In addition, the corners of the natural collision zones normally have structures different from those of linear mountain belts. For example, the geological/petrological characteristics and deep structures of the western and eastern Himalayan syntaxes are very different from those of the central Himalayas (e.g. Burg et al., 1997; Burg and Podladchikov, 1999, 2000; Zeitler et al., 2001; Yin, 2006; Burg and Schmalholz, 2008; Guillot et al., 2008; Oreshin et al., 2008). Therefore, 3-D numerical
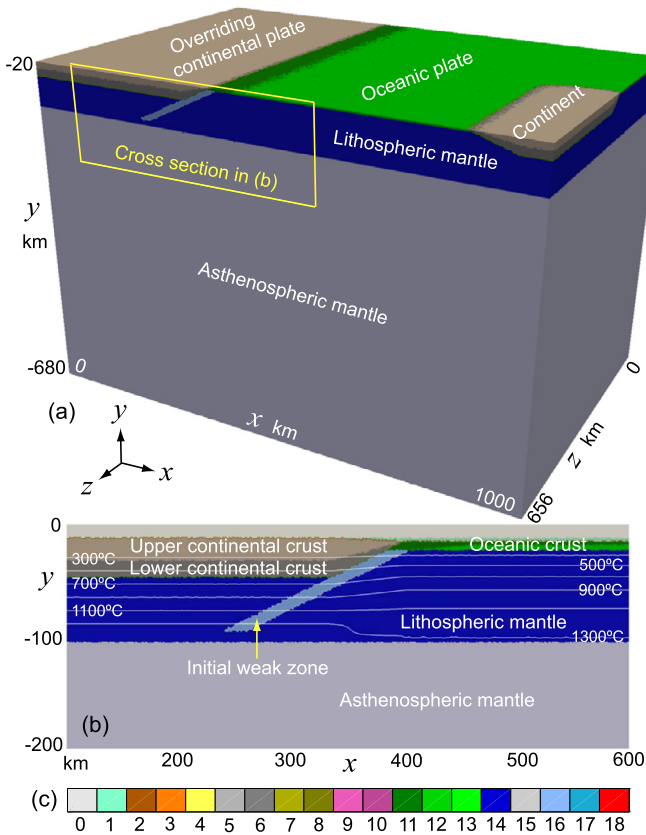
Fig. 1. Initial model configuration. (a) The 3-D model domain ($1000 \times 680 \times 656$ km, Fig. 1) with colors indicating different rock types as in (c). The top layer ($y > -20$ km) is cut off for clarity. (b) The zoomed domain of the subduction zone as shown in (a). White lines are isotherms measured in °C. (c) The colorgrid for different rock types, with: 0-air; 1-water; 2, 3-sediment; 4-partial molten sediment; 5/6-upper/lower continental crust; 7/8-hydrated upper/lower continental crust; 9/10-partial molten upper/lower continental crust; 11/12-upper/lower oceanic crust; 13-partial molten oceanic crust; 14-lithospheric mantle; 15-asthenospheric mantle; 16/17-hydrated/serpentinized mantle; 18-partially molten mantle. The hydrated and partially molten rocks are not shown in Fig. 1, but will appear during the evolution of the model (e.g., Figs. 2 and 3). Detailed properties of different rock types are shown in Tables S2 and S3 in the supplementary Appendix.

models are necessary to investigate such three-dimensional problems (e.g., Van Hunen and Allen, 2011).

In this paper we aim investigating the dynamics during collision of continental corners by conducting 3-D high-resolution numerical simulations. After the description of numerical methodology and model setup, a series of 3-D numerical simulations with variable convergence velocities is presented. The results are then compared with the eastern Alpine–Himalayan Belt, which has involved transitions from oceanic subduction to continental collision. The comparison focuses on the occurrence and dynamics of extrusion tectonics around the western corner of the Arabia–Asia collision zone (e.g., McClusky et al., 2000; Sengor et al., 2005) and around the eastern corner of the India–Asia collision zone (e.g., Wang et al., 2001; Zhang et al., 2004). In addition, several important processes such as break-off of the oceanic slab, asthenospheric mantle return flow, and topography evolution in the 3-D collisional processes are discussed.

2. 3-D numerical modeling method

2.1. Numerical setup and boundary conditions

Large scale models ($1000 \times 680 \times 656$ km, Fig. 1) are designed for the study of dynamic processes during continental corner colli-

sion involving subduction of the lithospheric mantle. The Cartesian spatial domain is resolved by $501 \times 341 \times 165$ grid points with the resolution of 2×2 km in the x–y plane and 4 km in the along-strike z-direction. The lithological structure of the model is represented by a dense grid of about 330 million randomly distributed markers used for advecting various material properties and temperatures.

The velocity boundary conditions are free slip at the top ($y = 0$) and at both the front and back boundaries ($z = 0$ and 656 km). The left and right boundaries ($x = 0$ and 1000 km) use constant normal velocities (convergence) in x-direction, which define the material influx through these side walls. For the permeable lower boundary condition (e.g., Burg and Gerya, 2005; Gerya et al., 2008a; Li et al., 2010), an external outflux boundary implies constant normal velocity and zero shear stress conditions to be satisfied at ∼200 km below the base of the model domain. The external boundary condition allows global conservation of mass in the computational domain and is implemented by using the following limitation for velocity components at the lower boundary: $\partial V_x / \partial y = 0$, $\partial V_z / \partial y = 0$, $\partial V_y / \partial y = (V_{y_{\text{external}}} - V_y)/\Delta y_{\text{external}}$, where $\Delta y_{\text{external}}$ is the vertical distance from the lower boundary to the external boundary and $V_{y_{\text{external}}}$ is the constant normal velocity on the external boundary.

2.2. Material and thermal configuration

In the initial model setup, the overriding plate is homogeneous continent in the transverse z-direction. The subducting plate is composed of half continental (328 km wide) and half oceanic (328 km wide) lithospheres in z-direction (Fig. 1a), behind the oceanic-only subducting plate (656 km in z-direction and 500 km in x-direction). In the vertical section of the continental side (Fig. 1a and 1b) the initial material setup implies the 3-D transition from oceanic subduction to continental collision, which is similar to that of previous 2-D models (e.g., Gerya et al., 2008a; Li and Gerya, 2009; Li et al., 2011, 2012). In the continental domain, the initial material field incorporates a 35 km thick continental crust composed of 20 km upper crust and 15 km lower crust, resting on the 58 km lithospheric mantle and the subjacent 575 km asthenospheric mantle. The oceanic domain is comprised of an 8 km thick oceanic crust overlying the 82 km thick lithospheric mantle and the subjacent 575 km asthenospheric mantle. The viscous flow law of 'wet quartzite' describes the behavior of both the sediment and continental upper crust, while the 'Plagioclase An$_{75}$' represents the continental lower crust and the oceanic crust (Tables S2 and S3; Ranalli, 1995). Subduction initiation is imposed along a ∼10 km thick weak zone dipping ∼25° in the lithospheric mantle. This weak zone has a 'wet olivine' rheology in contrast to the 'dry olivine' rheology elsewhere in both the lithospheric and asthenospheric mantle. The rheological properties of hydrated and partially molten crustal and mantle rocks are shown in Tables S2 and S3.

The top surface of the lithosphere is calculated dynamically as an essentially internal free surface by using a buffer layer of 'sticky air' (Gerya and Yuen, 2003; Schmeling et al., 2008; Crameri et al., 2012). It is an initially 12–15 km thick layer above the upper crust, which changes dynamically during experiments. The composition is either "air" (1 kg/m^3, above $y = -12$ km water level) or "water" (1000 kg/m^3, below $y = -12$ km water level), which has a low viscosity (10^{19} Pa s). Crameri et al. (2012) found that the sticky air approach is adequate as long as the term $(\eta_{\text{st}}/\eta_{\text{ch}})/(h_{\text{st}}/L)^3$ is small, where η_{st} and h_{st} are the viscosity and thickness of the sticky air layer, and η_{ch} and L are the characteristic viscosity and length scale of the model, respectively. According to this criterion, the quality of the internal free-surface condition in our models is rather moderate. But further decrease

in the 'sticky air' viscosity and/or increase in its thickness are precluded by numerical limitations of the multigrid solver convergence. Indeed, the large viscosity contrast caused by this low-viscosity boundary layer minimizes shear stresses ($<10^5$ Pa) at the top of the solid portion of the model (Burg and Gerya, 2005). For simplicity, surface erosion and sedimentation are neglected, which is a first order approximation acceptable at the considered time and space scales.

The initial thermal structure of the subducting continental lithosphere (white lines in Fig. 1b) is laterally uniform with 0 °C at the surface ($\leqslant$12 km, the air) and 1327 °C at 100 km depth, with linear interpolation in between. The thermal structure of the overriding continental lithosphere is similar with 0 °C at the surface, but 1322 °C at 90 km depth (slightly warmer than the subducting continent). The relatively thin and hot continental lithosphere is applied in consistency with some mountain belts, such as Tibet (e.g., Owens and Zandt, 1997; Tilmann et al., 2003; Liang et al., 2012). The thermal structure of the oceanic lithosphere is applied using the half-space cooling age of 30 Ma (Turcotte and Schubert, 2002). The initial temperature gradient in the asthenospheric mantle is about 0.5 °C/km. The thermal boundary conditions have a fixed value (0 °C) for the upper boundary and zero horizontal heat flux across the vertical boundaries. For the lower thermal boundary, an infinity-like external constant temperature condition is imposed, which allows both temperatures and vertical heat fluxes to vary along the permeable lower boundary of the box. This implies that the constant temperature condition is satisfied at $\sim$200 km below the bottom of the model. This condition is implemented by using the equation $\partial T/\partial y = (T_{external} - T_y)/\Delta y_{external}$ at the lower boundary, where $T_{external}$ is the temperature at the external boundary and $\Delta y_{external}$ is the vertical distance from the lower boundary to the external boundary (e.g., Burg and Gerya, 2005; Gerya et al., 2008a; Li et al., 2010).

2.3. Hydration and melting implementation

In the numerical model, water is expelled from the subducted oceanic crust as a consequence of both dehydration reactions and compaction. Equilibrium mineralogical water content is calculated for the Lagrangian rock markers at every time step based on Gibbs free energy minimization (Connolly and Petrini, 2002; Connolly, 2005; Gerya and Meilick, 2011) as a function of the local pressure, temperature and rock composition. The additional connate water content of the basaltic, upper oceanic crust and sediment is assumed as a linear function of depth.

$$X_{H_2O(P)}(\text{wt.\%}) = X_{H_2O(P_0)}(1 - \Delta z/75) \tag{1}$$

where $X_{H_2O(P)} = 2$ wt.% is the connate water content at the surface, Δz (km) is the depth below the surface in kilometer (0–75 km). The release of water also mimics the effects of low-temperature ($T < 573$ K) reactions not included in our thermodynamic database. According to the numerical models, water released from the slab creates a rheologically weak, hydrated zone, which ensures self-sustaining retreating subduction (Gerya et al., 2008b). To simulate the migration of water released by dehydration process, we use independently moving rock and fluid markers (Gorczyk et al., 2007a). To account for water transport, a fluid marker with its water amount is generated and moves upward until it reaches a lithology that assimilates water. Following Nikolaeva et al. (2008) the velocity of water is computed as

$$v_{x(\text{water})} = v_x$$

$$v_{y(\text{water})} = v_y + v_{y(\text{percolation})}$$

$$v_{z(\text{water})} = v_z \tag{2}$$

where y is the vertical coordinate pointing upward, x and z are the horizontal coordinates, respectively; v_x, v_y and v_z indicate the local velocity, $v_{y(\text{percolation})} = 10$ cm/a, an assumed parameter (Peacock, 1990; Gorczyk et al., 2007b), characterizing the upward speed of free water through the mantle. The sensitivity tests of the percolation speed $v_{y(\text{percolation})}$ on our results are shown in the supplementary Appendix (Figs. S1, S2). Free water is consumed by hydration and melting reactions in the mantle. Consequently, the propagation of the hydration/melting front in the mantle wedge is limited by the availability of water. This propagation is thus related to the rate of subduction which brings water to depths (Gerya et al., 2006).

The degree of melting of hydrated peridotite is computed as a function of pressure, temperature and water content using the parameterization of Katz et al. (2003). The degree of melting of crustal rocks is calculated according to the simple linear melting model (Burg and Gerya, 2005; Gerya and Meilick, 2011; Li et al., 2011):

$$M = 0, \quad \text{when: } T \leqslant T_{solidus}$$

$$M = \frac{(T - T_{solidus})}{(T_{liquidus} - T_{solidus})}, \quad \text{when: } T_{solidus} < T < T_{liquidus}$$

$$M = 1, \quad \text{when: } T \geqslant T_{liquidus} \tag{3}$$

where M is the volumetric fraction of melt with temperature T. $T_{solidus}$ and $T_{liquidus}$ are solidus temperature and dry liquidus temperature at a given pressure and temperature, respectively (Table S3; Ranalli, 1995).

Consequently, the effective density, ρ_{eff}, of partially molten rocks varies with the amount of melt fraction and P–T conditions according to the relations:

$$\rho_{eff} = \rho_{solid} - M(\rho_{solid} - \rho_{molten}) \tag{4}$$

where ρ_{solid} and ρ_{molten} are the densities of the solid and molten crustal rock, respectively, which vary with pressure and temperature according to the relation:

$$\rho_{P,T} = \rho_0 \big[1 - \alpha(T - T_0)\big]\big[1 + \beta(P - P_0)\big] \tag{5}$$

where ρ_0 is the standard density at $P_0 = 0.1$ MPa and $T_0 = 298$ K.

The effect of latent heating is implicitly included by increasing the effective heat capacity (Cp_{eff}) and thermal expansion (α_{eff}) of partially molten rocks ($0 < M < 1$), calculated as (Gerya, 2010):

$$Cp_{eff} = Cp + Q_L\left(\frac{\partial M}{\partial T}\right)_{P=\text{cnst}}$$

$$\alpha_{eff} = \alpha + \rho\frac{Q_L}{T}\left(\frac{\partial M}{\partial P}\right)_{T=\text{cnst}} \tag{6}$$

where Cp and α are the heat capacity and the thermal expansion of the solid crust, respectively, and Q_L is the latent heat of melting of the crust (Table S3).

2.4. Visco-plastic rheology

The relationships between the deviatoric stress (σ'_{ij}) and the strain rate ($\dot{\varepsilon}_{ij}$) tensors are described by the visco-plastic constitutive laws allowing for strain localization (e.g., Buiter et al., 2006; Ruh et al., 2013). In case of incompressible viscous deformation, the viscous law of friction is:

$$\sigma'_{xx} = 2\eta_{eff}\dot{\varepsilon}_{xx} \qquad \sigma'_{yy} = 2\eta_{eff}\dot{\varepsilon}_{yy} \qquad \sigma'_{zz} = 2\eta_{eff}\dot{\varepsilon}_{zz}$$

$$\sigma'_{xy} = 2\eta_{eff}\dot{\varepsilon}_{xy} \qquad \sigma'_{yz} = 2\eta_{eff}\dot{\varepsilon}_{yz} \qquad \sigma'_{xz} = 2\eta_{eff}\dot{\varepsilon}_{xz}$$

$$\dot{\varepsilon}_{xx} = \frac{\partial v_x}{\partial x} \qquad \dot{\varepsilon}_{yy} = \frac{\partial v_y}{\partial y} \qquad \dot{\varepsilon}_{zz} = \frac{\partial v_z}{\partial z}$$

$$\dot{\varepsilon}_{xy} = \frac{1}{2}\left(\frac{\partial v_x}{\partial y} + \frac{\partial v_y}{\partial x}\right) \qquad \dot{\varepsilon}_{yz} = \frac{1}{2}\left(\frac{\partial v_y}{\partial z} + \frac{\partial v_z}{\partial y}\right)$$

$$\dot{\varepsilon}_{xz} = \frac{1}{2}\left(\frac{\partial v_x}{\partial z} + \frac{\partial v_z}{\partial x}\right) \tag{7}$$

where η_{eff} is the effective viscosity that depends on the pressure, temperature, composition, strain rate and degree of melting.

The viscosity for ductile creep is defined by:

$$\eta_{\text{ductile}} = (\dot{\varepsilon}_{II})^{\frac{1-n}{n}}(A_D)^{-\frac{1}{n}}\exp\left(\frac{E+PV}{nRT}\right) \tag{8}$$

where $\dot{\varepsilon}_{II} = (0.5\dot{\varepsilon}_{ij}\dot{\varepsilon}_{ij})^{1/2}$ is the second invariant of the strain rate tensor and A_D, E, V and n are experimentally determined flow law parameters (Tables S1 and S2), which stand for material constant, activation energy, activation volume and stress exponent, respectively.

The ductile rheology is combined with a brittle/plastic rheology to yield an effective visco-plastic rheology. The Drucker–Prager yield criterion is easier to be implemented in 3-D than the Mohr–Coulomb criterion, while in 2-D these two criteria are known to be equivalent. Therefore the Drucker–Prager yield criterion (e.g., Ranalli, 1995) was implemented as follows:

$$\sigma_{\text{yield}} = C_0 + P\sin(\varphi_{eff})$$

$$\sin(\varphi_{eff}) = \sin(\varphi)(1-\lambda)$$

$$\eta_{\text{plastic}} = \frac{\sigma_{\text{yield}}}{2\dot{\varepsilon}_{II}} \tag{9}$$

where σ_{yield} is the yield stress, $\dot{\varepsilon}_{II}$ is the second invariant of the strain rate tensor, P is the dynamic pressure; C_0 is the residual rock strength at $P = 0$ and φ is the internal frictional angle; λ is the pore fluid coefficient that controls the brittle strength of fluid-containing porous or fractured media. φ_{eff} can be illustrated as the effective internal frictional angle that integrates the effects of internal frictional angle (φ) and pore fluid coefficient (λ). In this paper, $C_0 = 1$ MPa for all the rock types. Therefore the plastic rheology is implemented by different values of $\sin(\varphi_{eff})$ for different rock types (Table S3), which are chosen according to the same principles as in previous 2-D subduction/collision models (e.g., Gerya et al., 2008a; Li et al., 2011).

With η_{ductile} and η_{plastic}, the visco-plastic rheology is assigned to the model by means of a Christmas tree-like criterion, where the rheological behavior depends on the minimum viscosity (or differential stress) attained between the ductile and brittle/plastic fields (Ranalli, 1995).

$$\eta_{\text{creep}} = \min(\eta_{\text{ductile}}, \eta_{\text{plastic}}) \tag{10}$$

It is worth notifying that elasticity might affect lithospheric flexure in collision zone, however the general dynamics of continental subduction/collision and underlying mantle flow remain well established by the visco-plastic rheology (Gerya and Yuen, 2003, 2007).

2.5. Governing equations and numerical implementation

The momentum, continuity and heat conservation equations for a 3-D creeping flow are solved. Abbreviations and units are listed in Table S1.

(1) 3-D Stokes equations:

$$\frac{\partial \sigma'_{xx}}{\partial x} + \frac{\partial \sigma'_{xy}}{\partial y} + \frac{\partial \sigma'_{xz}}{\partial z} = \frac{\partial P}{\partial x}$$

$$\frac{\partial \sigma'_{yx}}{\partial x} + \frac{\partial \sigma'_{yy}}{\partial y} + \frac{\partial \sigma'_{yz}}{\partial z} = \frac{\partial P}{\partial y} - g\rho(C, M, P, T)$$

$$\frac{\partial \sigma'_{zx}}{\partial x} + \frac{\partial \sigma'_{zy}}{\partial y} + \frac{\partial \sigma'_{zz}}{\partial z} = \frac{\partial P}{\partial z} \tag{11}$$

(2) Conservation of mass is approximated by the incompressible continuity equation:

$$\frac{\partial v_x}{\partial x} + \frac{\partial v_y}{\partial y} + \frac{\partial v_z}{\partial z} = 0 \tag{12}$$

(3) Heat conservation equations:

$$\rho C_p\left(\frac{DT}{Dt}\right) = -\frac{\partial q_x}{\partial x} - \frac{\partial q_y}{\partial y} - \frac{\partial q_z}{\partial z} + H_r + H_a + H_S$$

$$q_x = -k\frac{\partial T}{\partial x} \qquad q_y = -k\frac{\partial T}{\partial y} \qquad q_z = -k\frac{\partial T}{\partial z}$$

$$H_a = T\alpha\frac{DP}{Dt}$$

$$H_S = \sigma'_{xx}\dot{\varepsilon}_{xx} + \sigma'_{yy}\dot{\varepsilon}_{yy} + \sigma'_{zz}\dot{\varepsilon}_{zz} + 2\sigma'_{xy}\dot{\varepsilon}_{xy} + 2\sigma'_{yz}\dot{\varepsilon}_{yz}$$
$$+ 2\sigma'_{xz}\dot{\varepsilon}_{xz} \tag{13}$$

where y is the vertical coordinate pointing upward, x and z are the horizontal coordinates (Fig. 1); v_x, v_y, and v_z indicate the components of the velocity vector; t is time; σ'_{ij} are the components of the viscous deviatoric stress tensor; $\dot{\varepsilon}_{ij}$ are the components of the strain rate tensor; g is the gravitational acceleration, and the density ρ depends explicitly on composition (C), melt fraction (M), temperature (T) and pressure (P). k is the variable thermal conductivity (Clauser and Huenges, 1995), C_p is the effective isobaric heat capacity, i.e., incorporating latent heat; H_r, H_a and H_S denote radioactive heat production (Table S3), the energetic effect of isothermal (de)compression (i.e., adiabatic heating/cooling), and shear heating, respectively.

The above equations are solved in the 'I3ELVIS' code (Gerya and Yuen, 2007; Zhu et al., 2009; Gerya, 2010) based on finite-differences with a marker-in-cell technique, which allows for non-diffusive numerical simulation of multiphase flow in a rectangular fully staggered Eulerian grid.

3. Model results

Series of numerical experiments were conducted with various convergence velocities V_c. The partition of V_c is that $V_c = V_{xo} - V_{xs}$, where V_{xo} is applied on the boundary plane $x = 0$ km (overriding side), and V_{xs} on the boundary plane of $x = 1000$ km (subducting side; Fig. 1). In Models-I and -II, $V_c = 5$ cm/a ($V_{xo} = 1.5$ cm/a, $V_{xs} = -3.5$ cm/a) for the first 10 Ma, which rules the oceanic subduction of 500 km. The partition of V_{xs}/V_{xo} was determined in order to keep the subduction/collision zone in the middle of the model domain, far from the boundaries in x-direction. The ratio V_{xs}/V_{xo} might affect the model evolution to a certain degree (Burov et al., in press). However, we emphasize that it does not change the general structures of the numerical models in a system with neglected inertia (Fig. S3). Then the convergence velocity was decreased linearly during continental subduction (10–15 Ma) to 2.5 cm/a for Model-I (Figs. 2a, 3a) and to 1 cm/a for Model-II (Fig. 6a). In Models-III and -IV, constant convergent velocities of 5 cm/a ($V_{xo} = 1.5$ cm/a, $V_{xs} = -3.5$ cm/a; Fig. 7a) and 3.0 cm/a ($V_{xo} = 1$ cm/a, $V_{xs} = -2$ cm/a; Fig. 8a) were applied, respectively. The configurations and detailed parameters are shown in Fig. 1 and Tables S2 and S3.

3.1. Reference Model-I

At the initial stages of our reference Model-I, the relatively strong oceanic plate subducted along the prescribed weak zone
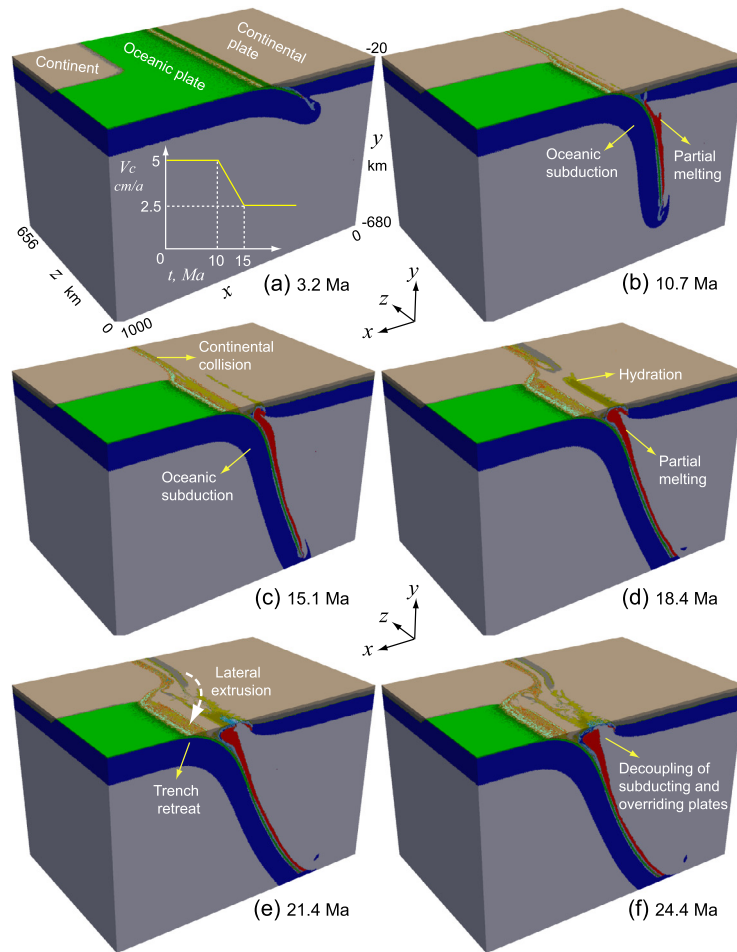
Fig. 2. Evolution of the reference model viewed in the oceanic subduction side. The top layer ($y > -20$ km) is cut off for clarity. The prescribed convergence velocity (V_c) decreases from 5 to 2.5 cm/a during the continental subduction (10–15 Ma) as shown in (a). The partition of V_c is that $V_c = V_{xo} - V_{xs}$, where $V_{xo} = 1.5$ cm/a (in the initial model) is applied on the boundary plane $x = 0$ km (overriding side), and $V_{xs} = -3.5$ cm/a on the boundary plane of $x = 1000$ km (subducting side). The ratio V_{xs}/V_{xo} is kept constant during the slowing of convergence. Colors of rock types are as in Fig. 1. Time (Ma) of shortening is given in the figures.

into the mantle (Figs. 2a–b, 3a–b). Water is expelled from the subducted oceanic crust as a consequence of both dehydration reactions and compaction (e.g., Zhu et al., 2009), which creates a rheologically weak hydrated zone in the mantle wedge closely above the subducting plate. The released water is transported into the mantle wedge and contributes to partial melting of the mantle (e.g., Figs. 2b–d). Viewed from the ocean-only side (Fig. 2), subduction is continuous while the trench retreats. The subducting plate becomes decoupled from the overriding plate (Figs. 2d–f). This process opens space for emplacement of partially molten material and mantle upwelling. At the same time, the side carrying continent has a different mode (Fig. 3). The incoming continental margin subducts to >100 km depth following the earlier oceanic subduction (Figs. 3b–c). Then, slab break-off occurs at about 150 km depth. After break-off of the oceanic slab, the subducted continental plate up-bends towards a shallower dip angle (cf., Figs. 3e and 3f), which is comparable to what happens after break-off in analogue models of continental collision (Chemenda et al., 2000). This event triggers exhumation of the subducted continental crustal rocks (Figs. 3d–e). Exhumation is similar to material circulation shown in previous numerical models of rheologically weak subduction channels (e.g., Burov et al., 2001; Stöckhert and Gerya, 2005; Yamato et al., 2007; Warren et al., 2008). Partially molten rocks, derived from both the continental crust and the mantle wedge, accumulate at the bottom of the overriding lithosphere (Figs. 3e–f). One of the most important phenomena is material lateral extrusion (in z-direction) from the con-

tinental collision side to the oceanic subduction side (Figs. 2e–f, 3e–f). Fig. 3 also displays the topography evolution, which indicates that the relief of the continental collision mountain can reach 5–6 km in the overriding plate over a wide area (Figs. 3d–f).

Comparing Figs. 2 and 3 discloses the differences between the oceanic subduction and the continental collision sides. The 1000 °C isotherm contour was plotted to make obvious the 3-D structure of the subducting slab (Fig. 4). On the oceanic side, subduction and trench retreat continue. By contrast, slab break-off occurs on the continental side in such a manner that the lateral integrity of the already subducted oceanic plate remains preserved (Fig. 4). Firstly, break-off initiates away from the continent corner, close to the free-slip side model boundary, at a site that can be regarded as the interior of the continent because of the mirror symmetry effect of free-slip condition in fluid dynamics (e.g., Li and Ribe, 2012). Then break-off propagates sideways in the z-direction towards the continental edge (lateral continental/oceanic transition zone) and finally propagates along the lateral edge of the subducted continental mantle lithosphere, in the x-direction. The slab window opens wider during break-off propagation in the y-direction, below the collided continents (Figs. 4c–d). The slab separated from the subducted continent continues subducting with the oceanic plate (Figs. 4c–d). The part of the plate remained attached to the subducted continent up-bends to a shallower dip angle (slab pull has ceased) during the growth of the 'tear' window (Figs. 4c–d).

In order to better define the slab break-off and to track the material flow, the effective viscosity and velocity fields were vi-
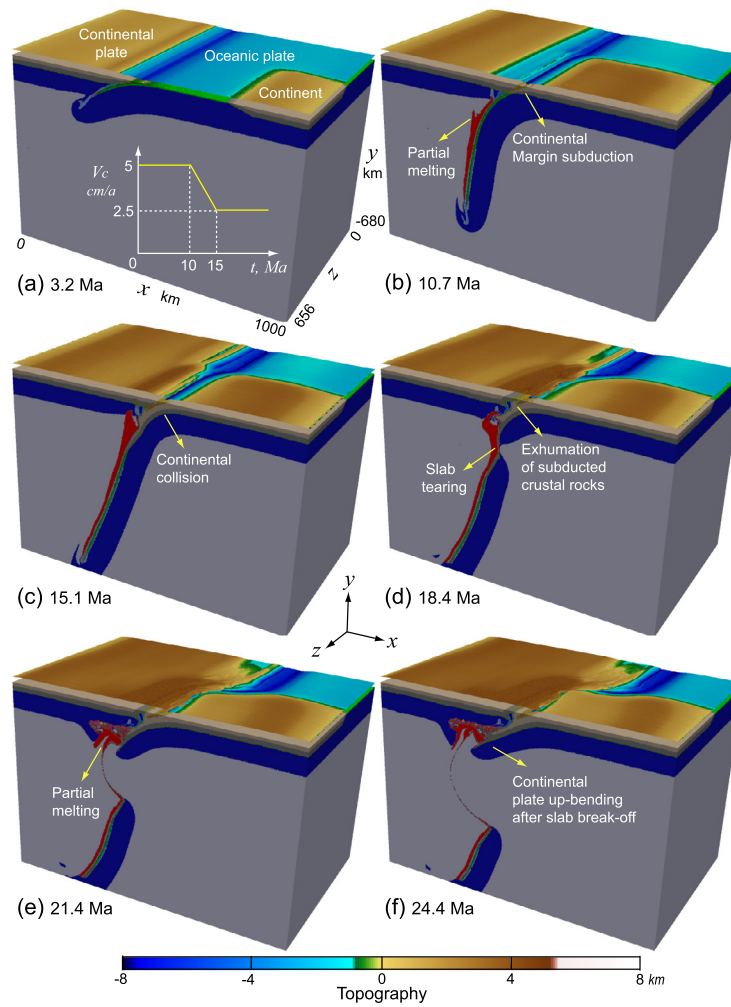
Fig. 3. Evolution of the reference model (same as Fig. 2) viewed in the continental collision side. The topography evolution is shown with the color scale in below.
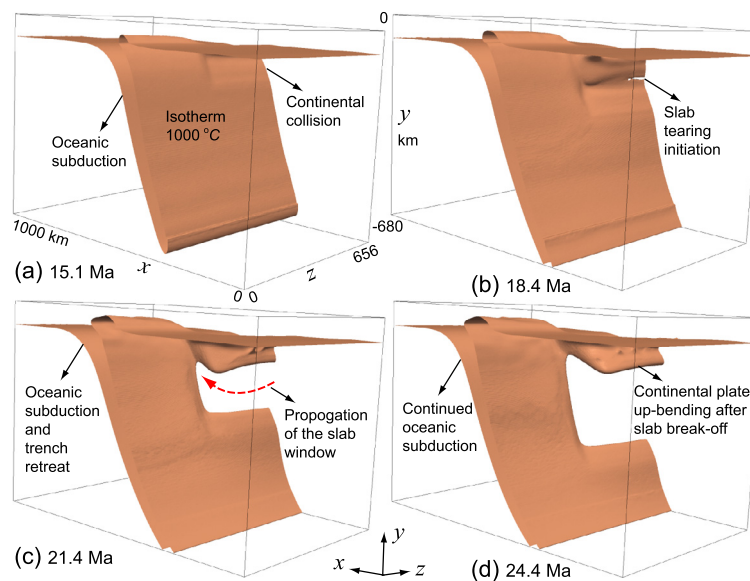

Fig. 4. 3-D Illustration of the subducting plate during slab break-off process, with the 1000 °C isotherm. The slab starts breaking near the lateral free-slip boundary on the continental collision side ($z = 656$ km), and the 'tear' is then propagating along-strike towards the continental edge (i.e., lateral continental/oceanic transition zone).

sualized (Fig. 5). They display how slab break-off evolves and the different styles of continental vs oceanic subduction. The surface velocity field demonstrates escape tectonics with material moving from the continental collision side to the oceanic subduction side (Figs. 5b, e). It also shows that extrusion velocity at the surface can be larger than the convergence velocity (Figs. 5b, e). The man-
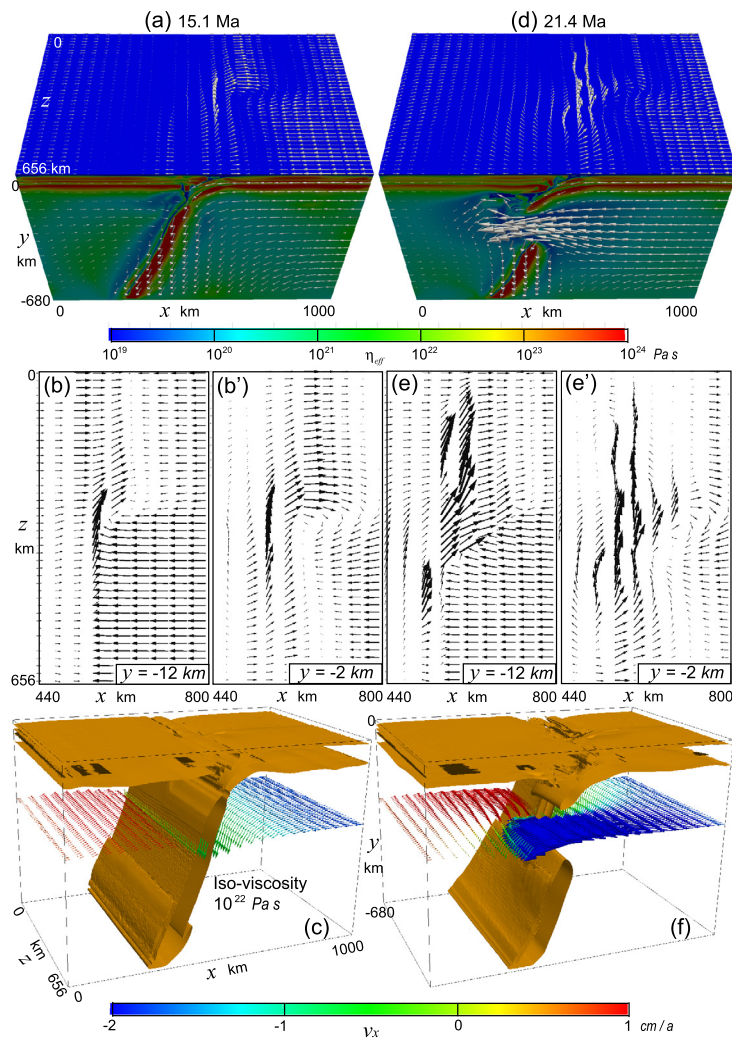
Fig. 5. The effective viscosity (η_{eff}) and velocity (v) field at two stages: (a–c) 15.1 Ma, and (d–f) 21.4 Ma. (a, d) show η_{eff} and v for the whole model domain. (b, e) demonstrate the velocity filed on a horizontal plane $y = -12$ km, which is the upper surface of the continent in the initial model, i.e. the boundary between the continent and the 'sticky air' (Fig. 1). (b', e') show the velocity field on a horizontal plane $y = -2$ km, for comparison. (c, f) plot a 3-D iso-viscosity contour ($\eta_{eff} = 10^{22}$ Pa s). The arrows show the velocity field on a horizontal plane ($y = -240$ km), with the colors indicating the component of velocity in the x-direction v_x.

tle velocity field specifies the flux of asthenospheric mantle from below the subducting slab of the collision zone, through the slab window to the mantle wedge (Figs. 5d, f). The mantle flux then turns around the corner area and accompanies the oceanic subduction and trench retreat (Fig. 5f). This mantle flow field is consistent with the '3-D edge flow' described in other models of laterally limited slabs (e.g., Funiciello et al., 2006; Piromallo et al., 2006; Schellart, 2008; Zandt and Humphreys, 2008; Li and Ribe, 2012). Flux directions in the deep mantle (Fig. 5f) are consistent with those on the surface (Fig. 5e), which are always from the continental collision towards the oceanic subduction side.

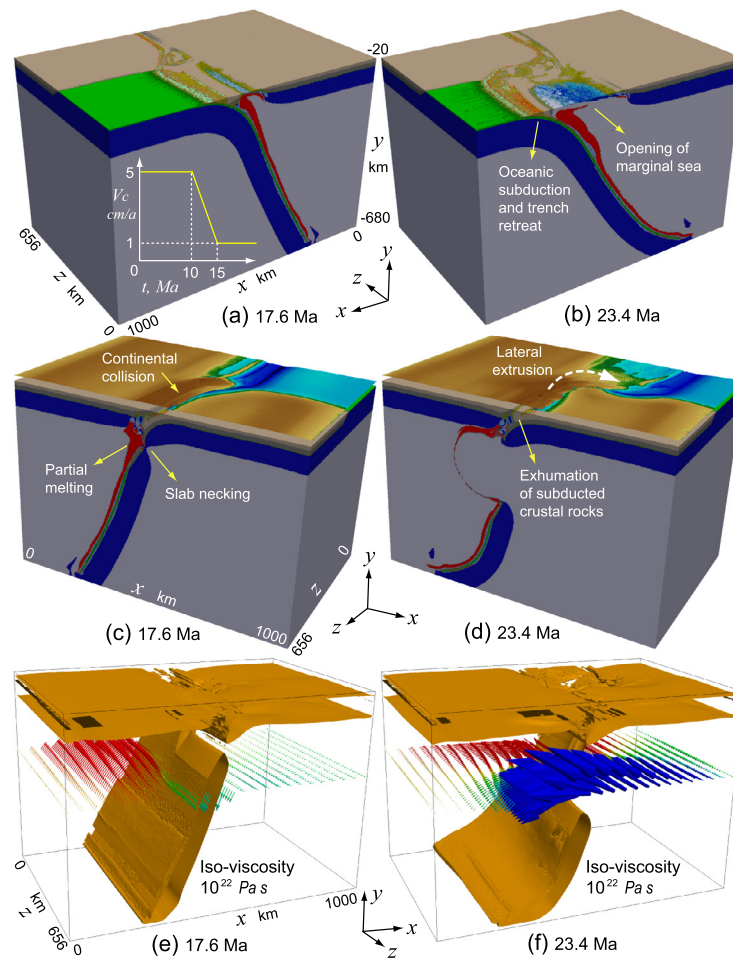### 3.2. Model-II: slow continental collision

In Model-II, the prescribed convergence velocity (V_c) decreases from 5 to 1 cm/a during continental subduction (10–15 Ma, Fig. 6a). Therefore this model simulates larger convergence deceleration and slower collision rate than reference Model-I.

The general results of Model-II are similar to those of Model-I: (1) oceanic subduction and trench retreat are continuous with hydrated weak zone and partially molten rocks developed in the mantle wedge, closely above the subducting plate (Figs. 6a, b); (2) tearing of the slab after continental collision with exhumation of the subducted continental crust (Figs. 6c, d); and (3) lateral

crustal extrusion from the collisional zone to the oceanic subduction side (Figs. 6b, d) along with mantle flux through the slab window from below the slab of the continental side towards the mantle wedge (Fig. 6f). However, since post-collision convergence is slow (1.0 cm/a after 15 Ma), the oceanic trench retreats relatively faster, opening a basin behind a rapidly retreating continental arc (Fig. 6b). Accordingly, the mantle flux through the slab window is faster than in Model-I (cf., Figs. 6f and 5f). Mantle flow further results in full decoupling between the subducting and the overriding plates (Fig. 6b). Break-off on the collision side occurs at shallower depth than in Model-I ($\leqslant 100$ km instead of ca 150 km; Figs. 6c and 3d). Crustal escape (i.e., lateral extrusion) in the overriding plate from the continental collision to the oceanic subduction side is faster, compensating the fast oceanic trench retreat (Figs. 6b, d). The high topography, which can reach about 5–6 km (Figs. 6c–d) during and after slab break-off, is localized near the collision zone. Significant back-arc extension and marginal-sea opening are worth noting in this model system (Fig. 6b).

3.3. Model-III: fast continental collision

In Model-III, the prescribed convergence velocity (V_c) keeps a constant value of 5 cm/a during the whole evolution from oceanic

Fig. 6. The model with prescribed convergence velocity (V_c) decreasing from 5 to 1 cm/a during the continental subduction (10–15 Ma) as shown in (a). The partition of V_c is the same as in the reference model (Fig. 2), where $V_{xo} = 1.5$ cm/a and $V_{xs} = -3.5$ cm/a at the beginning, and the V_{xs}/V_{xo} ratio is kept constant during the collision. (a–b) View in the oceanic subduction side. Colors of rock types are as in Fig. 1. (c–d) View in the continental collision side. The topography color scale is the same as in Fig. 3. (e–f) Iso-viscosity ($\eta_{eff} = 10^{22}$ Pa s) with the velocity field on a horizontal plane ($y = -240$ km). The velocity (v_x) color scale is the same as in Fig. 5. Time (Ma) of shortening is given in the figures.

subduction to continental collision (Fig. 7a). This model represents fast collision.

In Model-III, the position of the oceanic trench is rather stable (Figs. 7a, b). Consequently the mantle flux through the slab window is slower than in Models-I and -II (Figs. 7e, 5f and 6f). This produces coupling between the subducting oceanic plate and the overriding continental plate (Figs. 7a, b). The incoming continental plate subducts deeper than in Models-I and -II with slab tearing at about 250–300 km depth (Fig. 7c). After slab separation, the subducted part of the plate carrying continent up-bends as in the reference Model-I (Figs. 7d, 3f). In this fast convergent regime, the topography of the overriding continent is high over a wide area (Fig. 7d), in marked contrast to the localized high topography near the collision zone in the slow collision regime of Model-II (Fig. 6d).

3.4. Model-IV: slow oceanic subduction

Like Model-III, Model-IV was conducted with a constant but slower (3 cm/a) convergence velocity throughout the whole model evolution (Fig. 8a). This model was designed to investigate the influence of slow oceanic subduction.

The model yielded similar results as those from reference Model-I: (1) continuous subduction of the oceanic side with slow trench retreat; (2) slab torn apart on the continental collision side, at a depth of about 150 km, which leads to exhumation of continental crust; and (3) lateral material flow both in the

deep asthenospheric mantle and in the shallower crust of the overriding plate. The main difference is that the subducted continental plate does not up-bend after break-off (Fig. 8d). Instead, the overriding plate tends to bend down and subduct also (so-called two-sided or ablative subduction; e.g., Faccenda et al., 2008; Li et al., 2011). This drag-down of the overriding plate is attributed to strong coupling between the subducting and overriding mantle lithospheres (Faccenda et al., 2008; Li et al., 2011).

4. Discussion

The subduction/collision of 3-D continental corners differs markedly from the general 2-D continental collision. In 2-D models, the material is confined in a vertical x–y plane, without along-strike deformation (e.g., Li et al., 2011). In the current 3-D models, lateral extrusion occurs in the overriding crust from continental collision to the oceanic subduction side. The deeper mantle flow, after slab break-off, has also a large component in the along-strike z-direction. In addition, the 3-D numerical models provide significant insights on the combined oceanic subduction and continental collision. On the oceanic subduction side, the plate continues subducting and retreating with the trench retreat rate depending on the prescribed boundary convergence velocity (faster convergence, slower retreat). On the continental collision side, slab tearing and break-off occurs when the continental plate has subducted to a
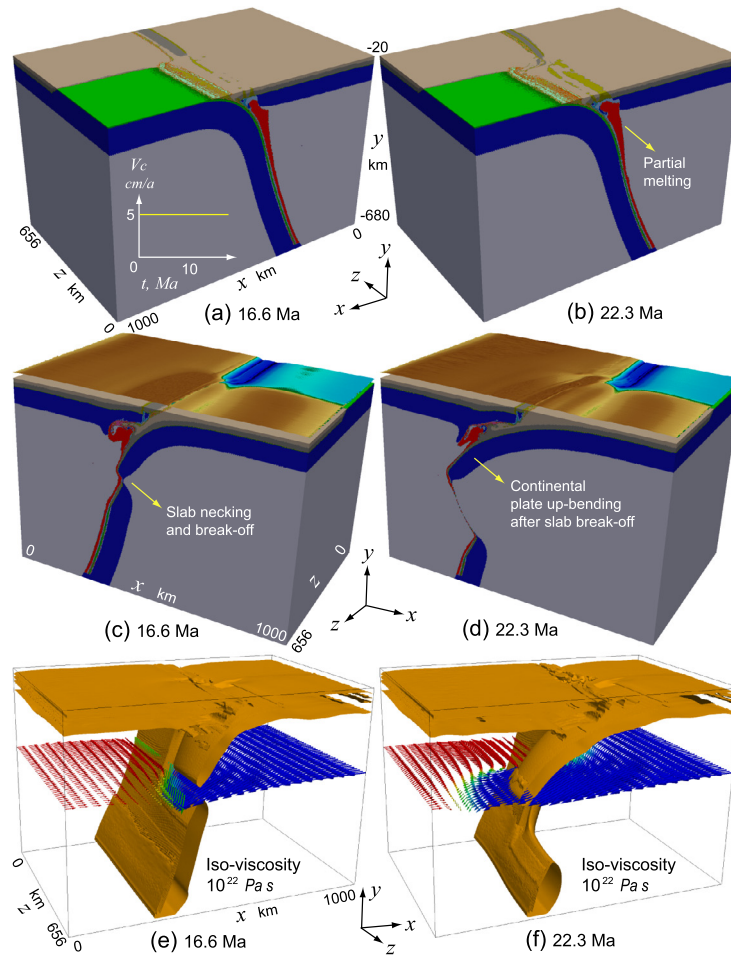
Fig. 7. The model with constant convergence velocity ($V_c = 5$ cm/a) as shown in (a). The partition of V_c is the same as in the reference model (Fig. 2), where $V_{xo} = 1.5$ cm/a and $V_{xs} = -3.5$ cm/a. (a–b) View in the oceanic subduction side. Colors of rock types are as in Fig. 1. (c–d) View in the continental collision side. The topography color scale is the same as in Fig. 3. (e–f) Iso-viscosity ($\eta_{eff} = 10^{22}$ Pa s) with the velocity field on a horizontal plane ($y = -240$ km). The velocity (v_x) color scale is the same as in Fig. 5. Time (Ma) of shortening is given in the figures.

depth that is positively correlated to the convergence velocity (faster convergence, larger depth).

The following discussion is organized around the principal aims of this study, which are (1) 3-D slab break-off dynamics, (2) lateral extrusion mechanism, and (3) implications for the eastern Alpine–Himalayan belt.

4.1. Three-dimensional slab break-off

The concept of slab tearing and break-off comes from interpretations of geophysical/geochemical observations in the subduction/collision zones, e.g., the positive seismic velocity anomalies interpreted as detached slab segments under India and the Himalayas (Van der Voo et al., 1999) and in the Mediterranean region (Wortel and Spakman, 2000). As summarized in Duretz et al. (2012), slab break-off has two major consequences: (1) partial or complete loss of the slab pull force and (2) inflow of hot asthenosphere where the slab ruptured. The first consequence is commonly used to explain tectonic processes such as surface uplift (Rogers et al., 2002), orogenic extension (Zeck, 1996) and exhumation of high pressure rocks (Andersen et al., 1991; Xu et al., 2010). The second consequence is usually considered to be an efficient mechanism for advecting heat at lithospheric to sub-crustal level, which triggers partial melting and plutonism (e.g., Davies and von Blanckenburg, 1995; Ferrari, 2004; Liu and Stegman, 2012).

Slab break-off has already been investigated by several analytical (e.g., Schmalholz, 2011), analogue (e.g., Regard et al., 2008) and numerical models (e.g., Davies and von Blanckenburg, 1995; Ton and Wortel, 1997; Buiter et al., 2002; Gerya et al., 2004; Toussaint et al., 2004; Burkett and Billen, 2010; Van Hunen and Allen, 2011; Duretz et al., 2011, 2012). 2-D numerical simulations (Duretz et al., 2011) demonstrate variable end-members, i.e. shallow ($\sim$40 km depth), intermediate ($\sim$200 km) and deep ($\sim$300 km) slab break-off. In our numerical models, the relationship between depth of slab break-off (D) and convergence velocity during continental collision (V_c) is: (1) shallow break-off ($D \leqslant 100$ km; Fig. 6c, $V_c = 1$ cm/a), (2) intermediate break-off ($D = \sim$150 km; Figs. 3d, 8c, $V_c = 2.5$–3 cm/a), and (3) deep break-off ($D = 250$–300 km; Fig. 7c, $V_c = 5$ cm/a). These results are consistent with 2-D simulations (Duretz et al., 2011), but the convergence rate in our 3-D models is applied by both 'ridge push' and 'slab pull', while it is only 'slab pull' in the referenced 2-D models. Recent 3-D models (Van Hunen and Allen, 2011) have shown that break-off propagates parallel to the trench, which can be either from somewhere within the slab to its edges in a symmetric collision setting, or from one edge to within the slab in an asymmetric setting. The dominant deformation mechanism during break-off is considered to be viscous necking (e.g., Schmalholz, 2011; Van Hunen and Allen, 2011; Duretz et al., 2012).

In our 3-D models, slab break-off is initiated away from the continental corner, at the free-slip model boundary (e.g., Fig. 4b), which actually would be within the continental plate. The 3-D
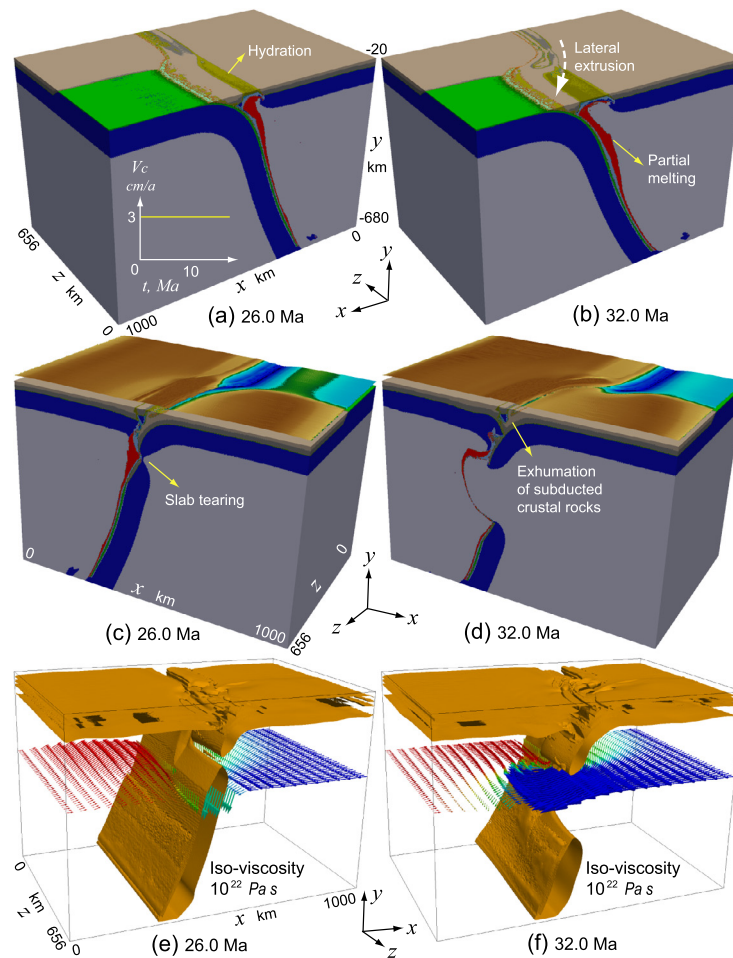
Fig. 8. The model with constant convergence velocity ($V_c = 3$ cm/a) as shown in (a), where $V_{xo} = 1$ cm/a and $V_{xs} = -2$ cm/a. (a–b) View in the oceanic subduction side. Colors of rock types are as in Fig. 1. (c–d) View in the continental collision side. The topography color scale is the same as in Fig. 3. (e–f) Iso-viscosity ($\eta_{eff} = 10^{22}$ Pa s) with the velocity field on a horizontal plane ($y = -240$ km). The velocity (v_x) color scale is the same as in Fig. 5. Time (Ma) of shortening is given in the figures.

style of slab break-off agrees with the results of Van Hunen and Allen (2011), but the trench-parallel tear propagation is limited by the cornered ocean-continent boundary. There, the tear does not propagate into the oceanic slab. Instead, it turns along the lateral continent boundary. In this system, the integrated slab pull is transmitted into the retreating oceanic subduction domain.

Our 3-D numerical simulations indicate that slab break-off plays fundamental roles in the dynamics of continental (corner) collision: (1) up-bending of the subducted continental plate after loss of slab pull along the former ocean-continent boundary (Figs. 3f, 7d), which does not appear in Model-IV (Fig. 8d) because of the tendency of two-sided subduction under coupled, high stress regime; (2) topography uplift in the collision zone (Fig. 3); and (3) asthenospheric mantle flow through the tear window (Fig. 5).

4.2. Lateral extrusion mechanism

Lateral extrusion was obtained in all models (Figs. 2, 6, 7 and 8), which suggests that escape tectonics is a common feature to all colliding continental corners. Comparing the models, lateral extrusion appears to depend on three factors:

(1) Continental collision and topography build-up; there is no lateral extrusion before onset of continental collision (Figs. 2a, 2b, 3a, 3b). Collision produces the necessary topography and gravitational potential, which can be regarded as a 'source' for material extrusion (e.g., Royden et al., 2008).

(2) Positive correlation with the trench retreat rate; faster trench retreat results in faster lateral extrusion (Fig. 6b). Conversely, slower trench retreat leads to slower extrusion (Fig. 7b). The intermediate trench retreat rate produces intermediate lateral material extrusion (Figs. 2f, 8b). Trench retreat causes extension in the upper plate, which provides a 'sink' region to receive the extruded materials.

(3) Slab break-off and mantle flow through the slab window (e.g., Fig. 5), which together facilitate trench retreat, hence lateral extrusion. Lateral extrusion expresses the link between deep mantle dynamics and crustal processes.

It is worth noting that surface processes, i.e. erosion and sedimentation, may influence the lateral extrusion to a certain degree. However their rates and scales are too small to change the general structure and dynamics of the continental collision (e.g., Li and Gerya, 2009). For the sake of simplicity, they were both neglected in the present models.

4.3. Implications for the eastern Alpine–Himalayan belt

The Alpine–Himalayan belt is one of the youngest and best documented continental convergent zones, which formed after closure of the Tethys Ocean. The eastern part of this convergent belt (Fig. 9) is composed of two continental collision zones alternating with three oceanic subduction zones (e.g., Vernant et al., 2004; Hatzfeld and Molnar, 2010; Yin, 2010): (1) the oceanic subduction
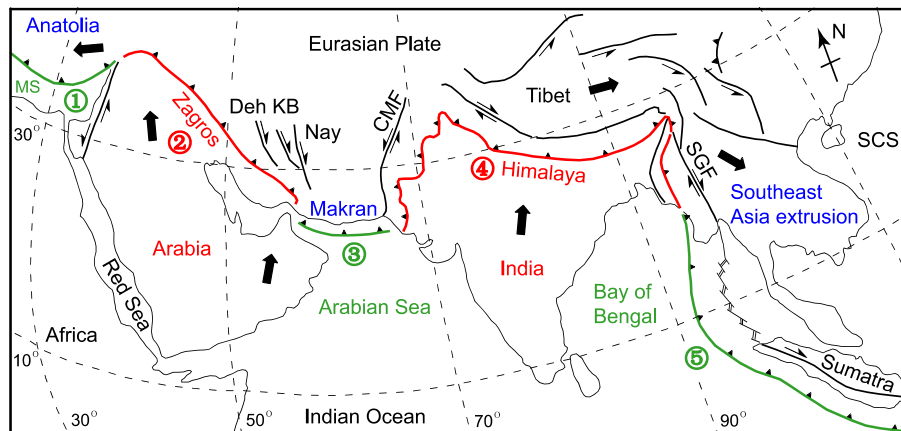
Fig. 9. Simplified tectonic map of the eastern Alpine–Himalayan belt (modified from Hatzfeld and Molnar, 2010; Yin, 2010; Xu et al., 2012). The green color shows the oceanic subduction zones. The red color indicates the continental collision zones. The blue color represents the lateral extrusion blocks in the overriding plate. The heavy black arrows indicate the movement of continental plates and the extrusion of the overriding continental rocks in the Eurasia-fixed reference frame, which are summarized from the GPS data (e.g., McClusky et al., 2000; Wang et al., 2001; Vernant et al., 2004; Zhang et al., 2004; Reilinger et al., 2010). MS: Mediterranean Sea; SCS: South China Sea; Deh: Dehshir Fault; KB: Kuh Banan Fault; Nay: Nayband Fault; CMF: Chaman Fault; SGF: Sagaing Fault. (For interpretation of the references to color in this figure caption, the reader is referred to the web version of this article.)

zone in the eastern Mediterranean Sea (MS), with the overriding Anatolian (western Turkey) plate being extruded westward; (2) the Arabia–Asia collision zone that produced the Zagros fold-thrust belt; (3) the Arabian Sea subduction under the Makran Accretionary Complex; (4) The South-Tibet–Himalaya thrust belt due to the India–Asia collision; and (5) the Indonesian oceanic subduction in the Bay of Bengal and Indian Ocean, with the east–southeastward extrusion of Asian blocks in the overriding plate. This orogenic system involves four continental corners, two symmetrical ones in front of Arabia, and two equally symmetrical in front of India. Due to computational limitations, we simulated collision of only one continental corner neighboring a piece of oceanic subduction zone, assuming that essential results can be applied to all natural cases through simple symmetry.

In the eastern Alpine–Himalayan belt, GPS data document lateral extrusion of Anatolia around the western corner of the Arabia–Asia collision zone (e.g., McClusky et al., 2000; Sengor et al., 2005; Reilinger et al., 2010), as well as escape of southeast Asia around the eastern corner of the India–Asia collision zone (e.g., Wang et al., 2001; Zhang et al., 2004). A dextral strike-slip fault system (Dehshir Fault, Kuh Banan Fault, Nayband Fault, Fig. 9) delineates the eastern side of the Arabia–Asia collision zone, accommodating northward penetration of Arabia into Asia. The sinistral Chaman fault system delimits the west-side of the India–Asia collision zone (Fig. 9), accommodating northward penetration of India into Asia. This pattern permits a relative southward extrusion of Iranian Blocks and the Makran Accretionary Complex between the two collision zones, but the GPS velocities are scarce over most parts of this region (e.g., Vernant et al., 2004; Hatzfeld and Molnar, 2010). Weaker extrusion of this eastern side compared to extrusion of Anatolia, in the west, may reflect narrow oceanic basins, thus limited subduction between the two collision belts (Fig. 9).

Extrusion of Anatolia is generally attributed to the Arabia–Asia collision as well as the southward retreat of the eastern Mediterranean subduction trench (e.g., Le Pichon and Angelier, 1979; Lister et al., 1984; Sengor et al., 2005; Ring et al., 2001; Hubert-Ferrari et al., 2002; Westaway, 2004; Marsellos and Kidd, 2008; Yin, 2010). On the one hand, trench retreat and the induced 'Aegean' extension could have facilitated lateral extrusion of Anatolia. On the other hand, northward penetration of the Arabia plate into Asia may have pushed the asthenosphere beneath Zagros in a counterclockwise flow pattern (e.g., Yin, 2010), which forced the eastern Mediterranean slab to retreat. Jolivet et al. (2013) also sug-

gest that extrusion of Anatolia is partly driven from below by the trench retreat induced asthenospheric flow (in agreement with the SKS fast directions) and partly from above by the extrusion of a lid of rigid crust (consistent with the stretching lineations in the crust). This association indicates connections between continental collision, oceanic trench retreat and lateral extrusion, as in our numerical models.

The extrusion of southeast Asia results from the ca 50 Ma old India–Asia collision (e.g., Tapponnier et al., 1982, 1986, 2001), which could either be the cause of marginal-sea opening such as the South China Sea (Fig. 9; e.g., Tapponnier et al., 1982; Peltzer and Tapponnier, 1988) or a result of trench retreat (e.g., Royden et al., 2008). Eastward lithospheric extrusion from central Tibet took place during a time of rapid trench rollback along much of the Pacific, Philippine, and Indonesian oceanic subduction boundaries (e.g., Tapponnier et al., 1986; van der Hilst and Seno, 1993). The Pacific and Philippine subduction, to the east of the southeast Asia extrusion system, is not included in either Fig. 9 or the numerical simulations. By contrast, the Indonesian subduction zone (Fig. 9) is treated as the oceanic subduction side in the numerical models (e.g., Fig. 2), which thereby plays a similar role as the eastern Mediterranean trench in the Anatolian extrusion system.

The scale of lateral extrusion around the corner of continent in the numerical models is about 200–300 km (Figs. 2, 5), which is smaller than the natural Anatolia and southeast Asia extrusion zones. The smallness of experimental extrusion is mainly attributed to the relatively small width of the models (656 km in z-direction) limited to that size because of the heavy computation in 3-D high-resolution numerical simulations. The model domain is laterally bounded by two free-slip vertical planes ($z = 0$ and 656 km), on which the normal velocity and shear stresses are zero. Therefore, material extrusion around the continental corner can only have a relatively small width, rather than moving laterally far away from the collision front. Although the computational limitation prevents reproducing the large size of laterally escaped blocks, the numerical models reveal similar geodynamical processes and provide significant insights into the mechanism of lateral extrusion tectonics. In addition, laterally heterogeneous structures (crustal thickness, thermal state, rheological structure, lithology, etc.) of different continental blocks may also play a major role in organization of 3-D patterns of plate tectonics in the eastern Alpine–Himalayan belt (Fig. 9). However numerical simulation of these factors is still prevented by the current computational limitations.

5. Conclusions

3-D numerical models of continental collision limited by a corner boundary with adjacent oceanic lithosphere simulated different, yet linked and coeval tectonic styles. The oceanic plate keeps subducting with trench retreat, without break-off. On the continental side, slab tearing and break-off occurs at a depth ($\leqslant$100 km to $\sim$300 km) related to the convergence velocity (faster convergence, larger depth). The slab tear window is first initiated away from the continental corner, then propagates along-strike to the edge of the continental plate, and finally, at a shallower depth, along the lateral continental/oceanic transition zone. The structures and dynamics of slab break-off are consistent with and further develop the previous 2-D and 3-D modes (e.g., Duretz et al., 2011; Van Hunen and Allen, 2011). Numerical experiments also simulate lateral extrusion tectonics and establish that it should be a general phenomenon during collision of continental corners. Lateral extrusion is driven both from above by the topography and gravitational potentials and from below by the trench retreat and asthenospheric mantle return flow.

Acknowledgements

Appendix A. Supplementary material

Supplementary material related to this article can be found online at http://dx.doi.org/10.1016/j.epsl.2013.08.034.

References

Andersen, T.B., Jamtveit, B., Dewey, J.F., 1991. Subduction and eduction of continental crust: major mechanisms during continent–continent collision and orogenic extensional collapse, a model based on the south Norwegian Caledonides. Terra Nova 3 (3), 303–310.

Beaumont, C., Jamieson, R.A., Nguyen, M.H., Lee, B., 2001. Himalayan tectonics explained by extrusion of a low-viscosity crustal channel coupled to focused surface denudation. Nature 414, 738–742.

Beaumont, C., Jamieson, R.A., Butler, J.P., Warren, C.J., 2009. Crustal structure: A key constraint on the mechanism of ultra-high-pressure rock exhumation. Earth Planet. Sci. Lett. 287, 116–129.

Boutelier, D., Chemenda, A.I., Jorand, C., 2004. Continental subduction and exhumation of high-pressure rocks: insights from thermo-mechanical laboratory modeling. Earth Planet. Sci. Lett. 222, 209–216.

Buiter, S.J.H., Govers, R., Wortel, M.J.R., 2002. Two-dimensional simulation of surface deformation caused by slab detachment. Tectonophysics 354, 192–210.

Buiter, S.J.H., Babeyko, A., Ellis, S., Gerya, T.V., Kaus, B.J.P., Kellner, A., Schreurs, G., Yamada, Y., 2006. The numerical sandbox: Comparison of model results for a shortening and an extension experiment. In: Buiter, S.J.H., Schreurs, G. (Eds.), Analogue and Numerical Modelling of Crustal-Scale Processes. In: Geol. Soc. London, Spec. Publ., vol. 253, pp. 29–64.

Burg, J.P., Davy, P., Nievergelt, P., Oberli, F., Seward, D., Diao, Z., Meier, M., 1997. Exhumation during crustal folding in the Namche Barwa syntaxis. Terra Nova 9, 117–123.

Burg, J.P., Podladchikov, Y., 1999. Lithospheric scale folding: numerical modelling and application to the Himalayan syntaxes. Int. J. Earth Sci. 88, 190–200.

Burg, J.P., Podladchikov, Y., 2000. From buckling to asymmetric folding of the continental lithosphere: numerical modelling and application to the Himalayan syntaxes. In: Geol. Soc. London, Spec. Publ., vol. 170, pp. 219–236.

Burg, J.-P., Gerya, T.V., 2005. The role of viscous heating in Barrovian metamorphism of collisional orogens: thermomechanical models and application to the Lepontine Dome in the Central Alps. J. Metamorph. Geol. 23, 75–95.

Burg, J.P., Schmalholz, S.M., 2008. Viscous heating allows thrusting to overcome crustal-scale buckling: Numerical investigation with application to the Himalayan syntaxes. Earth Planet. Sci. Lett. 274, 189–203.

Burkett, E.R., Billen, M.I., 2010. Three-dimensionality of slab detachment due to ridge–trench collision: Laterally simultaneous boudinage versus tear propagation. Geochem. Geophys. Geosyst. 11, Q11012.

Burov, E., Jolivet, L., Le Pourhiet, L., Poliakov, A., 2001. A thermomechanical model of exhumation of high pressure (HP) and ultra-high pressure (UHP) metamorphic rocks in Alpine-type collision belts. Tectonophysics 342, 113–136.

Burov, E., Francois, T., Yamato, P., Wolf, S., in press. Mechanisms of continental subduction and exhumation of HP and UHP rocks. Gondwana Res., http://dx.doi.org/10.1016/j.gr.2012.09.010.

Chemenda, A.I., Mattauer, M., Malavieille, J., Bokun, A., 1995. A mechanism for syn-collisional rock exhumation and associated normal faulting: Results from physical modeling. Earth Planet. Sci. Lett. 132, 225–232.

Chemenda, A.I., Mattauer, M., Bokun, A., 1996. Continental subduction and a mechanism for exhumation of high-pressure metamorphic rocks: new modelling and field data from Oman. Earth Planet. Sci. Lett. 143, 178–182.

Chemenda, A.I., Burg, J.-P., Mattauer, M., 2000. Evolutionary model of the Himalaya–Tibet system: geopoem based on new modelling, geological and geophysical data. Earth Planet. Sci. Lett. 174, 397–409.

Chen, L., Gerya, T.V., Zhang, Z.J., Aitken, A., Li, Z.H., Liang, X.F., 2013. Formation mechanism of steep convergent intracontinental margins: Insights from numerical modeling. Geophys. Res. Lett. 40, 2000–2005.

Clauser, C., Huenges, E., 1995. Thermal conductivity of rocks and minerals. In: Ahrens, T.J. (Ed.), Rock Physics and Phase Relations. In: Reference Shelf, vol. 3. American Geophysical Union, Washington, D.C., pp. 105–126.

Connolly, J.A.D., Petrini, K., 2002. An automated strategy for calculation of phase diagram sections and retrieval of rock properties as a function of physical conditions. J. Metamorph. Geol. 20, 697–708.

Connolly, J.A.D., 2005. Computation of phase equilibria by linear programming: A tool for geodynamic modeling and an application to subduction zone decarbonation. Earth Planet. Sci. Lett. 236, 524–541.

Crameri, F., Schmeling, H., Golabek, G.J., Duretz, T., Orendt, R., Buiter, S.J.H., May, D.A., Kaus, B.J.P., Gerya, T.V., Tackley, P.J., 2012. A comparison of numerical surface topography calculations in geodynamic modelling: an evaluation of the 'sticky air' method. Geophys. J. Int. 189, 38–54.

Davies, H.J., von Blanckenburg, F., 1995. Slab break-off: a model of lithosphere detachment and its test in the magmatism and deformation of collisional orogens. Earth Planet. Sci. Lett. 129, 85–102.

Duretz, T., Gerya, T.V., May, D.A., 2011. Numerical modelling of spontaneous slab break-off and subsequent topographic response. Tectonophysics 502, 244–252.

Duretz, T., Schmalholz, S.M., Gerya, T.V., 2012. Dynamics of slab detachment. Geochem. Geophys. Geosyst. 13, Q03020.

Faccenda, M., Gerya, T.V., Chakraborty, S., 2008. Styles of post-subduction collisional orogeny: Influence of convergence velocity, crustal rheology and radiogenic heat production. Lithos 103, 257–287.

Ferrari, L., 2004. Slab detachment control on mafic volcanic pulse and mantle heterogeneity in central Mexico. Geology 32, 77–80.

Funiciello, F., Moroni, M., Piromallo, C., Faccenna, C., Cenedese, A., Bui, H.A., 2006. Mapping mantle flow during retreating subduction: Laboratory models analyzed by feature tracking. J. Geophys. Res. 111, B03402.

Gerya, T.V., Yuen, D.A., 2003. Characteristics-based marker-in-cell method with conservative finite-differences schemes for modeling geological flows with strongly variable transport properties. Phys. Earth Planet. Inter. 140, 293–318.

Gerya, T.V., Yuen, D.A., Maresch, W., 2004. Thermomechanical modelling of slab detachment. Earth Planet. Sci. Lett. 226, 101–116.

Gerya, T.V., Connolly, J.A.D., Yuen, D.A., Gorczyk, W., Capel, A.M., 2006. Seismic implications of mantle wedge plumes. Phys. Earth Planet. Inter. 156, 59–74.

Gerya, T.V., Yuen, D.A., 2007. Robust characteristics method for modelling multiphase visco-elasto-plastic thermo-mechanical problems. Phys. Earth Planet. Inter. 163, 83–105.

Gerya, T.V., Perchuk, L.L., Burg, J.-P., 2008a. Transient hot channels: Perpetrating and regurgitating ultrahigh-pressure, high-temperature crust-mantle associations in collision belts. Lithos 103, 236–256.

Gerya, T.V., Connolly, J.A.D., Yuen, D.A., 2008b. Why is terrestrial subduction one-sided? Geology 36, 43–46.

Gerya, T.V., 2010. Introduction to Numerical Geodynamic Modelling. Cambridge University Press.

Gerya, T.V., Meilick, F.I., 2011. Geodynamic regimes of subduction under an active margin: effects of rheological weakening by fluids and melts. J. Metamorph. Geol. 29, 7–31.

Gorczyk, W., Gerya, T.V., Connolly, J.A.D., Yuen, D.A., 2007a. Growth and mixing dynamics of mantle wedge plumes. Geology 35, 587–590.

Gorczyk, W., Willner, A.P., Gerya, T.V., Connolly, J.A.D., Burg, J.-P., 2007b. Physical controls of magmatic productivity at Pacific-type convergent margins: Numerical modelling. Phys. Earth Planet. Inter. 163, 209–232.

Guillot, S., Maheo, G., de Sigoyer, D., Hattori, K.H., Pecher, A., 2008. Tethyan and Indian subduction viewed from the Himalayan high- to ultrahigh-pressure metamorphic rocks. Tectonophysics 451, 225–241.

Hatzfeld, D., Molnar, P., 2010. Comparisons of the kinematics and deep structures of the Zagros and Himalaya and of the Iranian and Tibetan plateaus and geodynamic implications. Rev. Geophys. 48, 2009RG000304.

Hubert-Ferrari, A., Armijo, R., King, G., Meyer, B., Barka, A., 2002. Morphology, displacement, and slip rates along the North Anatolian Fault, Turkey. J. Geophys. Res. 107 (B10), 2235.

Jolivet, L., Faccenna, C., Huet, B., et al., 2013. Aegean tectonics: Strain localisation, slab tearing and trench retreat. Tectonophysics 597–598, 1, http://dx.doi.org/10.1016/j.tecto.2012.06.011.

Katz, R.F., Spiegelman, M., Langmuir, C.H., 2003. A new parameterisation of hydrous mantle melting. Geochem. Geophys. Geosyst. 4, 1073.

Le Pichon, X., Angelier, J., 1979. Hellenic arc and trench system – key to the neotectonic evolution of the eastern Mediterranean area. Tectonophysics 60, 1–42.

Li, Z., Gerya, T., 2009. Polyphase formation and exhumation of HP-UHP rocks in continental subduction zone: Numerical modelling and application to the Sulu UHP terrane in eastern China. J. Geophys. Res. 114, B09406.

Li, Z.H., Gerya, T.V., Burg, J.P., 2010. Influence of tectonic overpressure on P-T paths of HP-UHP rocks in continental collision zones: thermomechanical modeling. J. Metamorph. Geol. 28, 227–247.

Li, Z.H., Xu, Z.Q., Gerya, T.V., 2011. Flat versus steep subduction: contrasting modes for the formation and exhumation of high- to ultrahigh-pressure rocks in continental collision zones. Earth Planet. Sci. Lett. 301, 65–77.

Li, Z.H., Xu, Z.Q., Gerya, T.V., 2012. Numerical geodynamic modeling of continental convergent margins. In: Dar, I.A. (Ed.), Earth Sciences. Pub. InTech, pp. 273–296.

Li, Z.-H., Ribe, N.M., 2012. Dynamics of free subduction from 3-D boundary-element modeling. J. Geophys. Res. 117, B06408.

Liang, X.F., Sandvol, E., Chen, Y.J., Hearn, T., Ni, J., Klemperer, S., Shen, Y., Tilmann, F., 2012. A complex Tibetan upper mantle: A fragmented Indian slab and no south-verging subduction of Eurasian lithosphere. Earth Planet. Sci. Lett. 333–334, 101–111.

Lister, G.S., Banga, G., Feenstra, A., 1984. Metamorphic core complexes of Cordilleran type in the Cyclades, Aegean Sea, Greece. Geology 12, 221–225.

Liu, M., Cui, X.J., Liu, F.T., 2004. Cenozoic rifting and volcanism in eastern China: a mantle dynamic link to the Indo-Asian collision? Tectonophysics 393, 29–42.

Liu, L., Stegman, D., 2012. Origin of Columbia River flood basalt controlled by propagating rupture of the Farallon slab. Nature 482, 386–389.

Marsellos, A.E., Kidd, W.S.F., 2008. Extension and exhumation of the Hellenic forearc ridge in Kythera. J. Geol. 116, 640–651.

McClusky, S., Balassanian, S., Barka, A., et al., 2000. Global positioning system constraints on plate kinematics and dynamics in the eastern Mediterranean and Caucasus. J. Geophys. Res. 105, 5695–5719.

Nikolaeva, K., Gerya, T.V., Connolly, J.A.D., 2008. Numerical modelling of crustal growth in intraoceanic volcanic arcs. Phys. Earth Planet. Inter. 171, 336–356.

Oreshin, S., Kiselev, S., Vinnik, L., Prakasamb, K.S., Rai, S.S., Makeyeva, L., Savvin, Y., 2008. Crust and mantle beneath western Himalaya, Ladakh and western Tibet from integrated seismic data. Earth Planet. Sci. Lett. 271, 75–87.

Owens, T.J., Zandt, G., 1997. Implication of crustal property variations for models of Tibetan plateau evolution. Nature 387, 37–43.

Peacock, S.M., 1990. Fluid processes in subduction zones. Science 248, 329–337.

Peltzer, G., Tapponnier, P., 1988. Formation and evolution of strike-slip faults, rifts, and basins during the India–Asia collision: an experimental approach. J. Geophys. Res. 93, 15,085–15,117.

Piromallo, C., Becker, T.W., Funiciello, F., Faccenna, C., 2006. Three-dimensional instantaneous mantle flow induced by subduction. Geophys. Res. Lett. 33, L08304.

Pope, D., Willett, C., 1998. Thermal–mechanical model for crustal thickening in the central Andes driven by ablative subduction. Geology 26 (6), 511–514.

Ranalli, G., 1995. Rheology of the Earth, Deformation and Flow Processes in Geophysics and Geodynamics, second ed. Chapman & Hall.

Regard, V., Faccenna, C., Bellier, O., Martinod, J., 2008. Laboratory experiments of slab break-off and slab dip reversal: insight into the Alpine Oligocene reorganization. Terra Nova 20 (4), 267–273.

Reilinger, R., McClusky, S., Paradissis, D., Ergintav, S., Vernant, P., 2010. Geodetic constraints on the tectonic evolution of the Aegean region and strain accumulation along the Hellenic subduction zone. Tectonophysics 488, 22–30.

Ring, U., Brachert, T., Fassoulas, C., 2001. Middle Miocene graben development in Crete and its possible relation to large-scale detachment faults in the southern Aegean. Terra Nova 13, 297–304.

Rogers, R.D., Karason, H., van der Hilst, R.D., 2002. Epeirogenic uplift above a detached slab in northern Central America. Geology 30 (11), 1031–1034.

Royden, R.H., Burchfiel, B.C., van der Hilst, R.D., 2008. The geological evolution of the Tibetan Plateau. Science 321, 1054–1058.

Ruh, J.B., Gerya, T., Burg, J.-P., 2013. High-resolution 3D numerical modeling of thrust wedges: Influence of decollement strength on transfer zones. Geochem. Geophys. Geosyst. 14 (4), 1131–1155, http://dx.doi.org/10.1002/ggge20085.

Sengor, A.M.C., Tuysuz, O., Imren, C., Sakinc, M., Eyidogan, H., Gorur, N., Le Pichon, X., Rangin, C., 2005. The north Anatolian fault: a new look. Annu. Rev. Earth Planet. Sci. 33, 37–112.

Schmeling, H., Babeyko, A.Y., Ennsa, A., et al., 2008. A benchmark comparison of spontaneous subduction models – Towards a free surface. Phys. Earth Planet. Inter. 171, 198–223.

Schmalholz, S.M., 2011. A simple analytical solution for slab detachment. Earth Planet. Sci. Lett. 304, 45–54.

Schellart, W.P., 2008. Kinematics and flow patterns in deep mantle and upper mantle subduction models: Influence of the mantle depth and slab to mantle viscosity ratio. Geochem. Geophys. Geosyst. 9, Q03014.

Schellart, W.P., Stegman, D.R., Farrington, R.J., Moresi, L., 2011. Influence of lateral slab edge distance on plate velocity, trench velocity, and subduction partitioning. J. Geophys. Res. 116, B10408.

Sobolev, S.V., Babeyko, A.Y., 2005. What drives orogeny in the Andes? Geology 33, 617–620.

Stöckhert, B., Gerya, T.V., 2005. Pre-collisional high pressure metamorphism and nappe tectonics at active continental margins: a numerical simulation. Terra Nova 17, 102–110.

Tao, W., O'Connell, R., 1992. Ablative subduction: a two-sided alternative to the conventional subduction model. J. Geophys. Res. 97 (B6), 8877–8904.

Tapponnier, P., Peltzer, G., Le Dain, A., Armijo, R., 1982. Propagating extrusion tectonics in Asia: New insights from simple experiments with plasticine. Geology 10, 611–616.

Tapponnier, P., Peltzer, G., Armijo, R., 1986. On the mechanics of the collision between India and Asia. In: Geol. Soc. London, Spec. Publ., vol. 19, pp. 115–157.

Tapponnier, P., Xu, Z., Roger, F., Meyer, B., Arnaud, N., Wittlinger, G., Yang, J., 2001. Oblique stepwise rise and growth of the Tibet Plateau. Science 294, 1671–1677.

Tilmann, F., Ni, J., INDEPTH III, 2003. Seismic imaging of the downwelling Indian lithosphere beneath central Tibet. Science 300, 1424–1427.

Ton, S.W.A., Wortel, M., 1997. Slab detachment in continental collision zones: an analysis of controlling parameters. Geophys. Res. Lett. 24 (16), 2095–2098.

Toussaint, G., Burov, E., Jolivet, L., 2004. Continental plate collision: unstable vs. stable slab dynamics. Geology 32, 33–36.

Turcotte, D.L., Schubert, G., 2002. Geodynamics, second ed. Cambridge University Press.

Van der Hilst, R., Seno, T., 1993. Effects of relative plate motion on the deep structure and penetration depth of slabs below the Izu-Bonin and Mariana island arcs. Earth Planet. Sci. Lett. 120, 395–407.

Van der Voo, R., Spakman, W., Bijwaard, H., 1999. Tethyan subducted slabs under India. Earth Planet. Sci. Lett. 171, 7–20.

Van Hunen, J., Allen, M., 2011. Continental collision and slab break-off: A comparison of 3-D numerical models with observations. Earth Planet. Sci. Lett. 302, 27–37.

Vernant, P., Nilforoushan, F., Hatzfeld, D., Abbassi, M., Vigny, C., Masson, F., Nankali, H., Martinod, J., Ashtiani, A., Bayer, R., Tavakoli, F., Chery, J., 2004. Present-day crustal deformation and plate kinematics in the Middle East constrained by GPS measurements in Iran and northern Oman. Geophys. J. Int. 157, 381–398.

Wang, Q., Zhang, P., Freymueller, J., Bilham, R., Larson, K., Lai, X., You, X., Niu, Z., Wu, J., Li, Y., Liu, J., Yang, Z., Chen, Q., 2001. Present-day crustal deformation in China constrained by global positioning system measurements. Science 294, 574–577.

Warren, C.J., Beaumont, C., Jamieson, R.A., 2008. Modelling tectonic styles and ultra-high pressure (UHP) rock exhumation during the transition from oceanic subduction to continental collision. Earth Planet. Sci. Lett. 267, 129–145.

Westaway, R., 2004. Kinematic consistency between the Dead Sea Fault Zone and the Neogene and Quaternary left-lateral faulting in SE Turkey. Tectonophysics 391, 203–237.

Wortel, M.J.R., Spakman, W., 2000. Subduction and slab detachment in the Mediterranean–Carpathian region. Science 290, 1910–1917.

Xu, W.-C., Zhang, H.-F., Parrish, R., Harris, N., Guo, L., Yuan, H.-L., 2010. Timing of granulite-facies metamorphism in the eastern Himalayan syntaxis and its tectonic implications. Geology 485, 231–244.

Xu, Z., Ji, S., Cai, Z., Zeng, L., Geng, Q., Cao, H., 2012. Kinematics and dynamics of the Namche Barwa Syntaxis, eastern Himalaya: Constraints from deformation, fabrics and geochronology. Gondwana Res. 21, 19–36.

Yamato, P., Agard, P., Burov, E., Le Pourhiet, L., Jolivet, L., Tiberi, C., 2007. Burial and exhumation in a subduction wedge: Mutual constraints from thermomechanical modeling and natural P-T-t data (Schistes Lustres, western Alps). J. Geophys. Res. 112, B07410.

Yamato, P., Burov, E., Agard, P., Le Pourhiet, L., Jolivet, L., 2008. HP-UHP exhumation during slow continental subduction: Self-consistent thermodynamically and thermomechanically coupled model with application to the Western Alps. Earth Planet. Sci. Lett. 271, 63–74.

Yin, A., 2006. Cenozoic tectonic evolution of the Himalayan orogen as constrained by along-strike variation of structural geometry, exhumation history, and foreland sedimentation. Earth-Sci. Rev. 76, 1–131.

Yin, A., 2010. Cenozoic tectonic evolution of Asia: A preliminary synthesis. Tectonophysics 488, 293–325.

Zandt, G., Humphreys, E., 2008. Toroidal mantle flow through the western U.S. slab window. Geology 36, 295–298.

Zeck, H.P., 1996. Betic-Rif orogeny: Subduction of Mesozoic Tethys lithosphere under eastward drifting Iberia, slab detachment shortly before 22 Ma, and subsequent uplift and extensional tectonics. Tectonophysics 254, 1–16.

Zeitler, P.K., Meltzer, A.S., Koons, P.O., Craw, D., Hallet, B., Chamberlain, C.P., Kidd, W., Park, S.K., Seeber, L., Bishop, M., Shroder, J., 2001. Erosion, Himalayan geo-dynamics, and the geomorphology of metamorphism. GSA Today 11 (1), 4–9.

Zhang, P., Shen, Z., Wang, M., Gan, W., Burgmann, R., Molnar, P., Wang, Q., Niu, Z., Sun, J., Wu, J., Hanrong, S., Xinzhao, Y., 2004. Continuous deforma-tion of the Tibetan Plateau from global positioning system data. Geology 32, 809–812.

Zhu, G., Gerya, T.V., Yuen, D.A., Honda, S., Yoshida, T., Connolly, J.A.D., 2009. 3-D dynamics of hydrous thermal–chemical plumes in oceanic subduction zones. Geochem. Geophys. Geosyst. 10, Q11006.